CHAPTER 8

Passive Radiative Cooling Applications for Thermal and Electrical Energy Harvesting

Ross Y. M. Wong
National Institute for Materials Science, Tsukuba, Japan

Christopher Y. H. Chao
The Hong Kong Polytechnic University, Hung Hom, Hong Kong, China

Satoshi Ishii
National Institute for Materials Science, Tsukuba, Japan

8.1 INTRODUCTION

Passive radiative cooling is a green technology without a carbon footprint that utilizes a sky-facing surface emitting thermal radiation through the bandwidth coincident with the infrared transparent atmospheric window lying within 8–13 μm of electromagnetic spectrum and self-preserving the temperature below ambient. It is deeply emerged in our daily life in which fog formation on land and plants under a nocturnal clear sky is a typical example. In 1978, with a titanium dioxide painted surface, it was the first time sub-ambient radiative cooling at daytime being reported in a scholarly research publication [1]. In 2014, thanks to escalating global concern on energy conservation and carbon neutrality, with a photonic radiative cooler composed of a bottom silver mirror and a top cascaded alternating silicon dioxide and hafnium dioxide 8–13 μm

DOI: 10.1201/9781003409090-8

thermal emitter, Raman et al.'s demonstration on daytime radiative cooling, realizing a temperature reduction of 5°C and a radiative cooling power of 40 W/m^2, drew intensive attention of the scientific community [2]. Then tremendous spectrally selective radiative coolers with improved thermal performance, broad materials selection, and scalable manufacturing feasibility were suggested within a few years [3–12]. They are expected to evolve numbers of engineering applications, especially for thermal and electrical systems. Aiming to review our latest developments on passive radiative cooling applications for thermal and electrical energy harvesting, this chapter is organized as follows. In Section 8.2 is a discussion of the analytical framework of thermo-photonic energy conversion for chilled water collection. Section 8.3 discusses one of the photo-thermoelectric energy conversion for electricity generation. In Section 8.4, is a discussion confronting the research challenge in passive radiative cooling. Last, Section 8.5 summarizes this chapter briefly. The advancement in radiative cooling materials is not discussed in this chapter because there have been a lot of published articles comprehensively reviewing the topic [13–15].

8.2 THERMO-PHOTONIC ENERGY CONVERSION FOR CHILLED WATER COLLECTION

A commercial chiller removes heat from chilled water via a vapor compression cycle, producing a cooling effect through a reversed Rankine cycle. A radiative-cooling-based chilled water system, simply integrable with a building's heating, ventilation, and air-conditioning system via a heat exchange interface, can substitute a part of the cooling load with a chiller and directly save electricity consumption. From the 1990s to 2000s, radiative-cooling-based chilled water systems were suggested and studied for nocturnal cooling capacity [16–21]. After Raman's succession in daytime radiative cooling, sub-ambient water cooling up to 5 °C during the daytime was demonstrated with a copper-tube-embedded aluminum plate exchanger [22]. Then a kilowatt scale radiative cooled cold collection system, also called RadiCool, was developed to chill water up to 10.6 °C at noon [23, 24]. Besides sensible cooling, water condensate can be harvested at the peak rate of 50 mL/m^2-hr through latent cooling [25, 26]. Building energy simulations and modeling predicted energy saving in office buildings by 45–68 % relative to variable air volume HVAC system [27], cooling electricity saving in two-floor single-family houses by 26–46 % relative to

split-type air conditioner [28], and indoor air temperature reduction up to 10 °C [29]. Unfortunately, chilling capacity of these radiative fluid cooling systems are bounded by a moderate radiative cooling power of 100 W/m^2. To efficiently utilize this new form of renewable energy resource, it is especially important to have a comprehensive understanding on their thermal and energy conversion performances, indicative by the fluid temperature reduction and energy conversion efficiency respectively.

Fluid temperature reduction denotes the fluid temperature difference before and after cooling, and energy conversion efficiency represents the ratio of enthalpy converted by the working fluid to the cooling effect harvestable from the sky [30]. To acknowledge the harvestable cooling effect, it is essential to consider energy balance of a radiative cooler subjected to a generic heat load q, which can be mathematically written as

$$P_{\mathrm{rad}}\left(T_{\mathrm{w}}\right)-P_{\mathrm{atm}}\left(T_{\mathrm{amb}}\right)-P_{\mathrm{sun}}-h_{\mathrm{c}}\left(T_{\mathrm{amb}}-T_{\mathrm{w}}\right)-\frac{q}{A}=0, \tag{8.1}$$

where T_{w} is the surface temperature, T_{amb} is the ambient temperature, h_{c} is the coefficient of heat transfer between the surface and the environment, and A is the surface area. At an arbitrary temperature T,

$$P_{\mathrm{rad}}\left(T\right)=\varepsilon\left(\lambda\right)I_{\mathrm{bb}}\left(\lambda,T\right)d\lambda\cos\theta d\Omega, \tag{8.2}$$

is the radiative heat flux emitted by the radiative cooling surface,

$$P_{\mathrm{atm}}\left(T\right)=\varepsilon\left(\lambda\right)\left[1-\tau_{\mathrm{atm},0}\left(\lambda\right)^{1/\cos\theta}\right]I_{\mathrm{bb}}\left(\lambda,T\right)d\lambda\cos\theta d\Omega, \tag{8.3}$$

is the radiative heat flux absorbed from the atmosphere, and,

$$P_{\mathrm{sun}}=\varepsilon\left(\lambda\right)I_{\mathrm{AM1.5G}}\left(\lambda\right)\cos\Psi d\lambda, \tag{8.4}$$

is the radiative heat flux absorbed from the sun, where $I_{\mathrm{bb}}(\lambda, T) = 2h_{\mathrm{p}}c^2/\lambda^5(e^{h_{\mathrm{p}}c/\lambda k_{\mathrm{b}}T} - 1)$ is the blackbody radiance, $c = 3 \times 10^8$ m/s is the speed of light, $h_{\mathrm{p}} = 6.63 \times 10^{-34}$ J-s is the Planck's constant, $k_{\mathrm{b}} = 1.38 \times 10^{-23}$ J/K is the Boltzmann constant, θ is the zenith angle of spherical coordinate system, Ω is the solid angle extending the upper hemisphere of spherical coordinate system, ψ is the zenith solar angle, λ is the wavelength,

$I_{AM1.5G}$ is the air mass 1.5 global solar radiance, ε is the spectral emissivity of radiative cooling surface, and $\tau_{atm,\,0}$ is the zenith atmospheric spectral transmittance.

When the surface temperature is raised to the ambient, the surface withstands the critical heat load that depends on ambient temperature only and equals the radiative cooling power in magnitude. Despite measuring the dischargeable electromagnetic energy, cooling power can be affected by materials properties, whereas harvestable cooling effect should be an intrinsic property of the sky as a heat dissipative thermal reservoir. Hence, cooling capacity should be determined by the ideal cooler capable in capturing the most cooling effect, performing as a spectrally selective blackbody emitter within 8–13 μm, but a perfect mirror elsewhere. Now energy conversion efficiency is well-defined as,

$$\eta_{th} = -\frac{\rho_f c_{p,f} Q_f \left(T_{f,c} - T_{f,h}\right)}{P_{net,ideal}\left(T_{amb}\right)}, \tag{8.5}$$

where ρ_f is the fluid density, $c_{p,\,f}$ is the specific heat capacity of fluid, Q_f is the flow rate of fluid, $T_{f,\,h}$ is the fluid temperature before cooling, $T_{f,\,c}$ is the fluid temperature after cooling, and $P_{net,\,ideal}(T_{amb})$ is the ideal radiative cooling power.

8.2.1 Energy Balance Model

To formulate the analytical framework for fluid temperature reduction and energy conversion efficiency, it is necessary to consider the 1-dimensional heat transfer model of a radiative fluid cooling system specified as follow. As shown in Figure 8.1(a) schematically, A rectangular channel of length l, width w, and height τ is engraved on a radiative cooler of area A. It connects two reservoirs at distinct temperatures of $T_{f,\,h}$ and $T_{f,\,c}$ respectively at the ends. Working fluid of density ρ_f and specific heat capacity $c_{p,\,f}$ drifts at a flow rate Q_f from the reservoir at $T_{f,\,h}$ to the one at $T_{f,\,c}$. Under uniform surface temperature T_w and adiabatic reservoir surfaces assumptions, an overall energy balance equation can be expressed as

$$P_{rad}\left(T_w\right) - P_{atm}\left(T_{amb}\right) - P_{sun} - h_c\left(T_{amb} - T_w\right) - \frac{\rho_f c_{p,f} Q_f}{A}\left(T_{f,h} - T_w\right) \times\left(1 - e^{-\frac{h_{fw} w l}{\rho_f c_{p,f} Q_f}}\right) = 0, \tag{8.6}$$

where h_{fw} is the fluid-wall interfacial heat transfer coefficient. In this equation, fluid-wall interfacial heat transfer is entirely contributed by forced convection in the closed channel and, in this circumstance, h_{fw} is dependent on the frontal area and mode of heating only and solvable by classical heat transfer theory. Numerical values of Nusselt number $Nu_{fw,\,D}$, the dimensionless form of h_{fw} equaling $Nu_{fw,\,D} = h_{fw}D_H/\kappa_f$, where κ_f is the thermal conductivity of fluid and D_H is the hydraulic diameter, are available in many heat transfer textbooks like ref. [31], ranging between 2.5 and 8.2 for fully developed laminar channel flow. Radiative fluid cooling performance is optimal upon satisfying the criteria of $h_{fw}wl/\rho_f c_{p,\,f}Q_f >> 1$. In this circumstance, eq. (8.6) can be further simplified by considering the system subjected to a small perturbation in fluid flow from Q_f to $Q_f + dQ_f$. The direct consequence is two-folded. First, T_w is shifted by dT_w. Second, overall energy balance reacts in two aspects, in which the heat currents, P_{rad} and $h_c(T_{amb} - T_w)$, are altered in response to the change in T_w. Then the differential energy response equation can be worked out by subtracting the energy balance equations at two different system statuses. And, recognizing the boundary conditions that saturation temperature reduction ΔT_∞ equals the unloaded temperature reduction and saturation energy conversion efficiency, $\eta_{th,\,\infty}$ vanishes as $Q_f \to 0$, as well as $\Delta T_\infty = 0$ and $\eta_{th,\,\infty} = 1$ as $Q_f \to \infty$, analytical expressions for ΔT_∞ and $\eta_{th,\,\infty}$ can be obtained by integration as,

$$\Delta T_\infty = -\frac{P_{net}\left(T_{amb}\right)}{\frac{\rho_f c_{p,f} Q_f}{A}\left(1+\frac{4E\left(T_{amb}\right)\sigma T_{amb}^3 A}{\rho_f c_{p,f} Q_f}+\frac{h_c A}{\rho_f c_{p,f} Q_f}\right)}, \tag{8.7}$$

and,

$$\eta_{th,\infty} = \frac{P_{net}\left(T_{amb}\right)}{P_{net,ideal}\left(T_{amb}\right)\left(1+\frac{4E\left(T_{amb}\right)\sigma T_{amb}^3 A}{\rho_f c_{p,f} Q_f}+\frac{h_c A}{\rho_f c_{p,f} Q_f}\right)}, \tag{8.8}$$

respectively, where $\sigma = 5.67 \times 10^{-8}$ W/m^2-K^4 is the Stefan Boltzmann constant and E is the ratio of the change in emitted radiative heat flux by a grey-body to a blackbody, and $P_{net}(T_{amb})$ is the radiative cooling power.

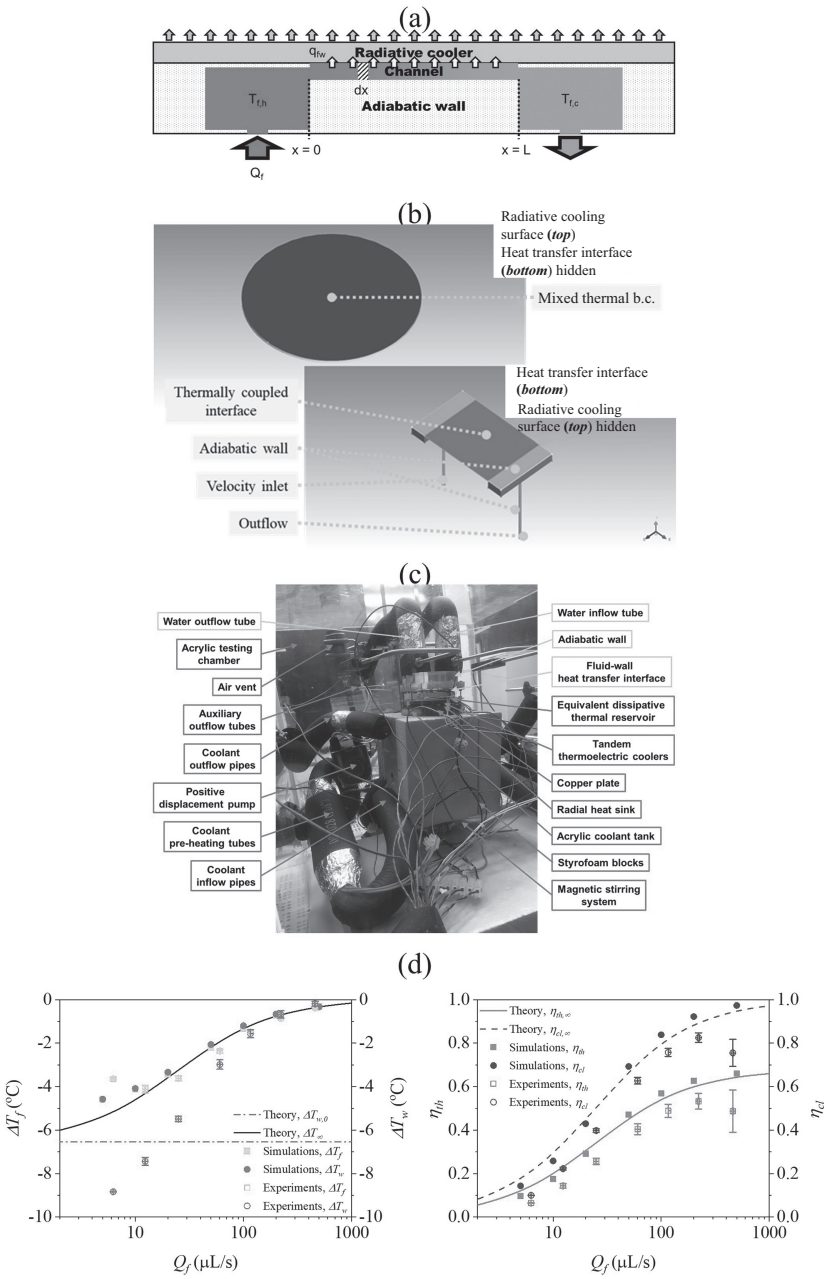

FIGURE 8.1 (a) one-dimensional heat transfer model; and (b) computational fluid dynamics simulation model for the passive radiative fluid cooling system; (c) a picture of the experimental setup for equivalent dissipative thermal reservoir experiment; a comparison of theoretical, simulated, and experimental results of (d) temperature reductions and efficiencies for flow rate between 2 μL/s and 1 mL/s

(*Continued*)

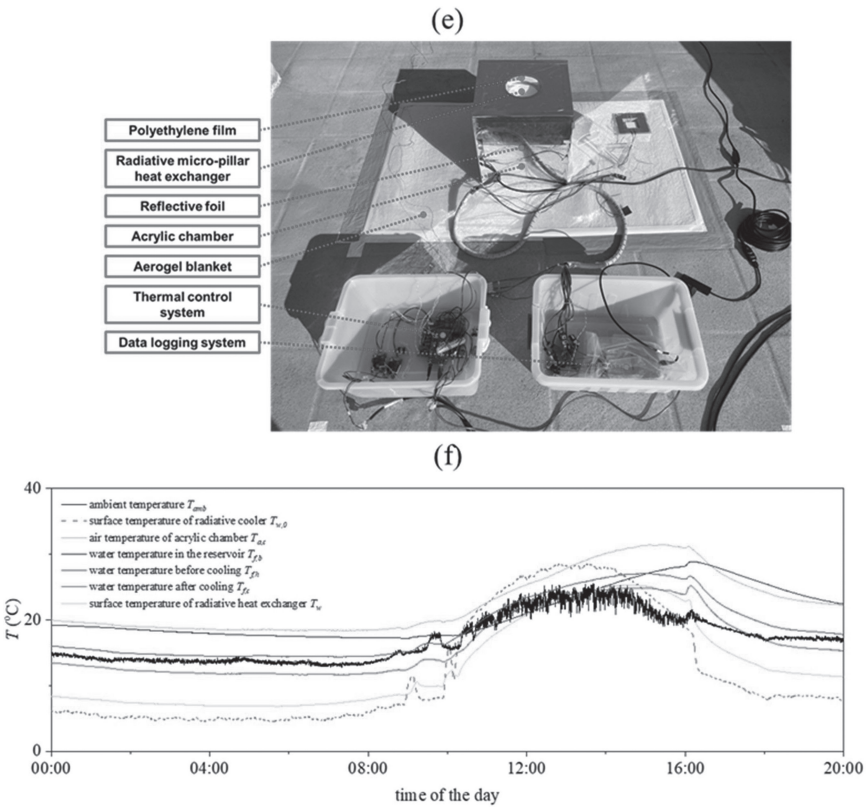

FIGURE 8.1 (*Continued*) (e) a picture of the experimental setup for outdoor field investigation on chilled water capacity; and (f) Daily profiles of measured system temperatures during outdoor field investigation on chilled water capacity. Part (c) is reprinted from *International Journal of Heat and Mass Transfer*, **174**, Corrected radiative cooling power measured by equivalent dissipative thermal reservoir method, 121341, Copyright (2021), with permission from Elsevier. Parts (c) and (d) are reprinted from *Renewable Energy*, **180**, Thermo-radiative energy conversion efficiency of a passive radiative fluid cooling system, 700 – 711, Copyright (2021), with permission from Elsevier. Parts (e) and (f) are reprinted from *International Journal of Heat and Mass Transfer*, **215**, Field demonstrated extended Graetzian viscous dissipative thermo-photonic energy conversion with a blended MgO/PVDF/PMMA coated glass-PDMS micro-pillar heat exchanger, 124520, Copyright (2023), with permission from Elsevier.

8.2.2 Computational Fluid Dynamics Simulations Model

Radiative fluid cooling performance can be demonstrated by computational fluid dynamics simulation. It involves two main procedures, including the meshing of computational domain and the iteration of discretized

governing equations under specified boundary conditions sequentially. As shown in Figure 8.1(b), the simulation model involves not only the fluid advancing space, but also the substrate for radiative cooling materials deposition, interconnected by a heat transfer interface. The model is decomposed into a finite number of elements with local refinement at the boundary faces and interface. For fluid sub-domain, the governing equations are given by the mass, momentum, and energy conservation equations which take the form of

$$\nabla \cdot \mathbf{v} = 0, \tag{8.9}$$

$$\rho_{\mathrm{f}}\left(\nabla \cdot \mathbf{v}\right)\mathbf{v} = -\nabla p + \nabla \cdot \boldsymbol{\tau}, \tag{8.10}$$

and,

$$\rho_{\mathrm{f}} c_{\mathrm{p,f}}\left(\nabla \cdot \mathbf{v}\right)T = \kappa_{\mathrm{f}} \nabla^2 T, \tag{8.11}$$

respectively for a single species, viscous and constant properties fluid, where $\boldsymbol{\tau} = \mu_{\mathrm{f}}(\nabla\,\mathbf{v} + \nabla\,\mathbf{v}^{\mathrm{T}})$ is the stress tensor, μ_{f} is the fluid viscosity, p is the hydrostatic pressure, $\mathbf{v}$ and $\mathbf{v}^{\mathrm{T}}$ are the fluid velocity vector and transpose of fluid velocity vector. Fluid velocity and temperature are specified at the inlet. Outflow boundary condition, where the gradients of flow variables are vanished, is employed at the outlet. And no-slip hydrodynamic boundary condition and adiabatic thermal boundary condition are applied on all surrounding walls. For solid sub-domain, mass and momentum transports are negligible, and energy transport is driven by conduction only, where the heat conduction equation can be written as

$$\nabla \cdot \left(\kappa_{\mathrm{s}} \nabla T\right) = 0, \tag{8.12}$$

where κ_{s} is the thermal conductivity of substrate. A mixed heat current, composed of a radiative current and a convective current, is specified at the radiative cooling surface. Thermally coupled wall condition is imposed at the fluid-wall heat transfer interface. An adiabatic wall boundary condition is set at the remaining walls. Finally, the governing equations are discretized by the second order upwind scheme, coupled with the SIMPLE algorithm, and solved by the finite element method. The relaxation factors are set in the range from 0.2 to 0.95. The discretized equations are iterated

until the normalized residues are reduced to 10^{-5} or below for mass and momentum conservation equation, and 10^{-9} or below for energy conservation equation.

8.2.3 Equivalent Dissipative Thermal Reservoir Experiment

Furthermore, radiative fluid cooling performance can be illustrated by equivalent dissipative thermal reservoir experiment. It makes use of the strong linear dependence of net radiative heat exchange between the radiative cooling surface and the environment when surface temperature and ambient temperature are slightly different. As such, fluid cooling performance can be examined under the replicated radiative cooling effect established by a linear free buoyant stream between the dummy radiative fluid cooling system and the equivalent dissipative thermal reservoir. As shown in Figure 8.1(c), the equivalent dissipative thermal reservoir at the effective temperature, constructed by a surface with the same area of dummy radiative cooling surface, was conducted to the cold side of a thermo-electrical cooling system. A copper plate, capping a heat exchanger, was channeled to the hot side. Coolant, kept at a constant temperature, was chilled and circulated by the refrigerative chillers. It took away residual heat pumped by the thermoelectric coolers upon execution. The two systems were mounted on a distance and orientation adjustable platform to set up the designated thermal boundary conditions. More details on the equivalent dissipative thermal reservoir experiment can be referred to ref. [32].

Figure 8.1(d) compares the theoretical, simulated, and measured surface temperature reduction, fluid temperature reduction, and energy conversion efficiency. Saturation temperature reduction decreases with flow rate, whereas saturation energy conversion efficiency increases with flow rate. At small flow rate of 2 μL/s, temperature reduction approaches the unloaded value of 6.5 °C, but efficiency falls to 0 %. At a large flow rate of 1 mL/s, temperature reduction declines to 0 °C, but efficiency climbs to the ideal limit of 100 %. This inversed correlation can also be captured by simulation and experiment. Simulated surface and fluid temperature reductions come to the same point. And experimental results show that water can be chilled by 4.1 °C and cooling effect can be harvested by 212 mW, equivalent to the energy conversion efficiency of 14 %, whereas water can be weakly chilled by 1.5 °C and cooling effect can be harvested by 726 mW, equivalent to an elevated efficiency of 49 %. For flow rate over 20 μL/s, these tendencies are coherent with the theoretical prediction. For flow rate below 20 μL/s, simulated and experimental results are distinguishable

from the analytical prediction. Despite the same simulated surface and fluid temperature reductions, the declining trends are not persistent with smaller flow rate and they plateau at 4.6 °C. Also, measured surface and fluid temperature reductions are not convergent. When the flow rate is 12.4 μL/s, fluid temperature reaches the bottom of 4.1 °C, higher than the saturation temperature reduction by 0.3 °C, but surface temperature reduction drops with flow rate continually, significantly lower than the saturation temperature reduction by 3 °C. As a consequence, energy conversion efficiency is lower than the saturation value.

8.2.4 Outdoor Field Investigation of Chilled Water Capacity

Furthermore, an outdoor field investigation of chilled water capacity was conducted with a wafer-sized radiative cooling blend coated glass-polydimethylsiloxane (glass-PDMS) micro-pillar heat exchanger [33]. The heat exchanger was composed of a micro-pillar patterned polydimethylsiloxane (PDMS) slab and a glass substrate. The PDMS slab was prepared by silicon stamping method [34, 35], in which the silicon master mask was fabricated by sequential micro-fabrication processes. PDMS, prepared by mixing the elastomer and curing agent in 10:1 was poured onto the patterned mask, baked in the oven for curing and lifted off from the mask after solidification. Lastly, a micro-porous radiative cooling blend was sprayed-coated on the opposite face. The blend was selected by recognizing the complementary thermal emissive property of poly(vinylidene-fluoride) and poly(methyl-methacrylate) through Maxwell-Garnett effective medium theory [36] and appraising the excellent solar reflective property of large energy bandgap dielectric materials [37–40]. Fourier transform mid-infrared spectrometry and UV/Vis/NIR spectrometry reveal high sky window emissivity and solar reflectivity.

As the experimental setup shown in Figure 8.1(e), the chilled water system, driven by a peristaltic pump, circulated water through the micro-pillar heat exchanger, water heating tube, and water reservoir at a constant flow rate of 6.3 μL/s. Besides, a radiative cooler with the same blend coated on a glass substrate was installed for radiative cooling power measurement. All components were well-insulated from conduction, convection, and radiation. Surface temperature of the radiative heat exchanger, water temperatures before and after cooling, as well as ambient temperature, were measured and their daily profiles were depicted in Figure 8.1(f). Beginning from sunset, the system arrived at different pseudo-steady temperatures at mid-night when the ambient temperature was 15.7 °C. Surface

temperature of the radiative heat exchanger lay at 7.7°C, and it chilled water from 17.1°C to 14.5°C, equivalent to surface and water temperature reductions by 8.0°C and 2.6°C respectively. At noon of the second day, ambient temperature climbed to 23.0°C. Surface temperature of the radiative heat exchanger remained near ambient at 22.8°C, and it chilled water from 24.2°C to 22.8°C, equivalent to surface and water temperature reductions by 0.2°C and 1.4°C respectively. At nighttime, cooling power was measured by loading the blend-coated radiative cooler to ambient temperature. Just before the measurement, ambient temperature and surface temperature of the radiative cooler were 15.0°C and 6.0°C respectively. This denoted an unloaded surface temperature reduction of 9.0°C. During the measurement, ambient temperature declined slightly from 15.9°C to 14.1°C and surface temperature followed the same trend. Averaged temperatures differed by 0.3°C due to thermal control error. In this scenario, it gave a cooling power of 131 W/m^2 on per area basis. Meanwhile, the radiative heat exchanger arrived at a surface temperature of 9.4°C and chilled water by 2.3°C. Hence, estimated cooling efficiency with these figures was 5.9 %.

Compared to the temperature reduction and efficiency predicted by Equations (8.7) and (8.8), measured values are significantly lower even though the system satisfies the saturation criteria, perhaps because, at such a small flow rate, axial heat conduction, neglected in the one-dimensional heat transfer model, can be comparative to the convective and interfacial heat currents. The interplay among these heat currents causes a loss of interfacial heat transfer, but an increase in internal viscous dissipation. As a result, it degrades overall chilled water capacity by passive radiative cooling in this flow regime.

8.3 PHOTO-THERMOELECTRICAL ENERGY CONVERSION FOR ELECTRICITY GENERATION

Photo-thermoelectrical generation is an equally important engineering application of passive radiative cooling technology. At daytime, in-site photo-electrical energy conversion can be simply realized by a photovoltaic cell. Nowadays, with a new anti-reflection coating, a concentrated multi-junction tandem solar cell made of III-V compounded semiconductors recorded the state-of-art solar-electrical energy conversion efficiency of 47.6 % [41]. At nighttime, similar direct renewable energy conversion technology was overlooked until recent attempts on photo-thermoelectricity generation enabled by radiative cooling. It makes use

of the heat dissipative radiative cooling coating to set up a temperature gradient between the hot and cold sides of a Peltier module and extract electrical work between the ambient and universe. Passive radiative-cooling based thermoelectrical energy harvesting has potential applications in various aspects, including building space cooling [42, 43], and powering wearable electronics [44, 45].

8.3.1 Energy Balance Model

Theoretically, system thermal performance, indicated by cold-sided temperature $T_{\mathrm{TE,\,c}}$ and hot-sided temperature $T_{\mathrm{TE,\,h}}$, can be acknowledged by solving the energy balance equations for the Peltier module of area A, comprising N p-n junctions with an individual Seebeck coefficient S_{pn}, thermal conductance K_{pn} and electrical resistance R_{pn}, connected to an external load of resistance R_{e}. For the cold side,

$$P_{\mathrm{rad}}\left(T_{\mathrm{TE,c}}\right)-P_{\mathrm{atm}}\left(T_{\mathrm{amb}}\right)-P_{\mathrm{sun}}-h_{\mathrm{c}}\left(T_{\mathrm{amb}}-T_{\mathrm{TE,c}}\right)-P_{\mathrm{cond}}\left(T_{\mathrm{TE,h}},T_{\mathrm{TE,c}}\right)-P_{\mathrm{seebeck}}\left(T_{\mathrm{TE,c}}\right)-P_{\mathrm{joule}}=0 \tag{8.13}$$

and, for the hot side,

$$-h_{\mathrm{c}}\left(T_{\mathrm{amb}}-T_{\mathrm{TE,h}}\right)+P_{\mathrm{cond}}\left(T_{\mathrm{TE,h}},T_{\mathrm{TE,c}}\right)+P_{\mathrm{seebeck}}\left(T_{\mathrm{TE,h}}\right)-P_{\mathrm{joule}}=0, \tag{8.14}$$

where $P_{\mathrm{cond}} = NK_{\mathrm{pn}}(T_{\mathrm{TE,\,h}} - T_{\mathrm{TE,\,c}})/A$ is the conductive heat flux, $P_{\mathrm{seebeck}} = NS_{\mathrm{pn}}TI/A$ is the Seebeck effect, $P_{\mathrm{joule}} = NI^2R_{\mathrm{pn}}/2A$ is the joule heating, and $I = NS_{\mathrm{pn}}(T_{\mathrm{TE,\,h}} - T_{\mathrm{TE,\,c}})/(NR_{\mathrm{pn}} + R_{\mathrm{e}})$ is the thermoelectrical current. In eq. (2.1), P_{rad}, P_{atm} and P_{sun} are given by Equations (8.2), (8.3) and (8.4) respectively and $h_{\mathrm{c}}(T_{\mathrm{amb}} - T_{\mathrm{TE,\,c}})$ is the non-radiative heat load from the environment. Hence, system electrical performance, denoted by thermoelectrical power output P_{e}, is coupled with the difference in $T_{\mathrm{TE,\,h}}$ and $T_{\mathrm{TE,\,c}}$ via I, and given by [46, 47]

$$P_{\mathrm{e}}=\frac{N^2S_{\mathrm{pn}}^2\left(T_{\mathrm{TE,h}}-T_{\mathrm{TE,c}}\right)^2R_{\mathrm{e}}}{\left(NR_{\mathrm{pn}}+R_{\mathrm{e}}\right)^2}. \tag{8.15}$$

An outdoor field investigation of the black-paint coated commercial thermoelectric module realized a two-sided temperature difference up to 2 °C and generated a thermoelectrical power of 25 mW/m^2 at the maximum

power point, in which the field investigative result validates the theoretical model [48]. Predicted thermoelectrical performance is divergent and highly sensitive to the input system parameters, in which Zhao et al. estimated a moderate output power density of 291 mW/m^2 [47], whereas Fan et al. forecasted a much larger optimal value of 2.2 W/m^2 [46].

8.3.2 Laboratory Testing on Thermo-Electricity Generation

A laboratory testing comparing thermo-electricity generation by Peltier modules combined with a selective thermal emitter and a blackbody thermal emitter was set up for duplicating thermo-electricity generation [49]. As shown in Figure 8.2(a), the selective thermal emitter was an e-beam evaporated 100 nm aluminum film on a glass with the glass side facing top, and the blackbody thermal emitter was a blackbody paint-sprayed glass with the blackbody paint facing top. Figure 8.2(b) shows their spectral emissivity and reflectivity from visible to mid-infrared wavelengths.

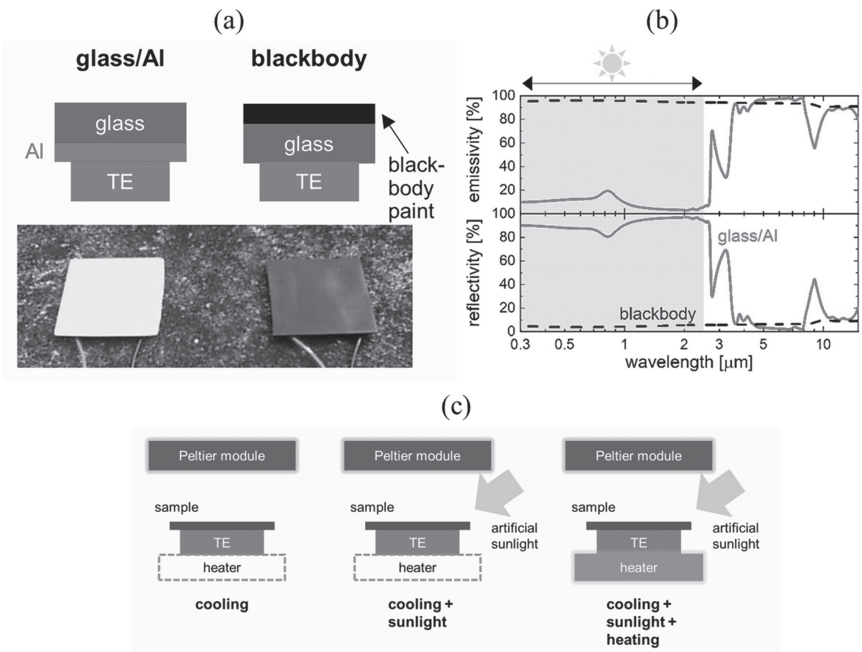

FIGURE 8.2 (a) Pictures of the selective and blackbody thermal emitters; (b) measured spectral emissivity and reflectivity of the selective and blackbody thermal emitters from visible light to mid-infrared wavelengths; (c) An illustrative diagram on the experimental conditions for laboratory testing

(*Continued*)

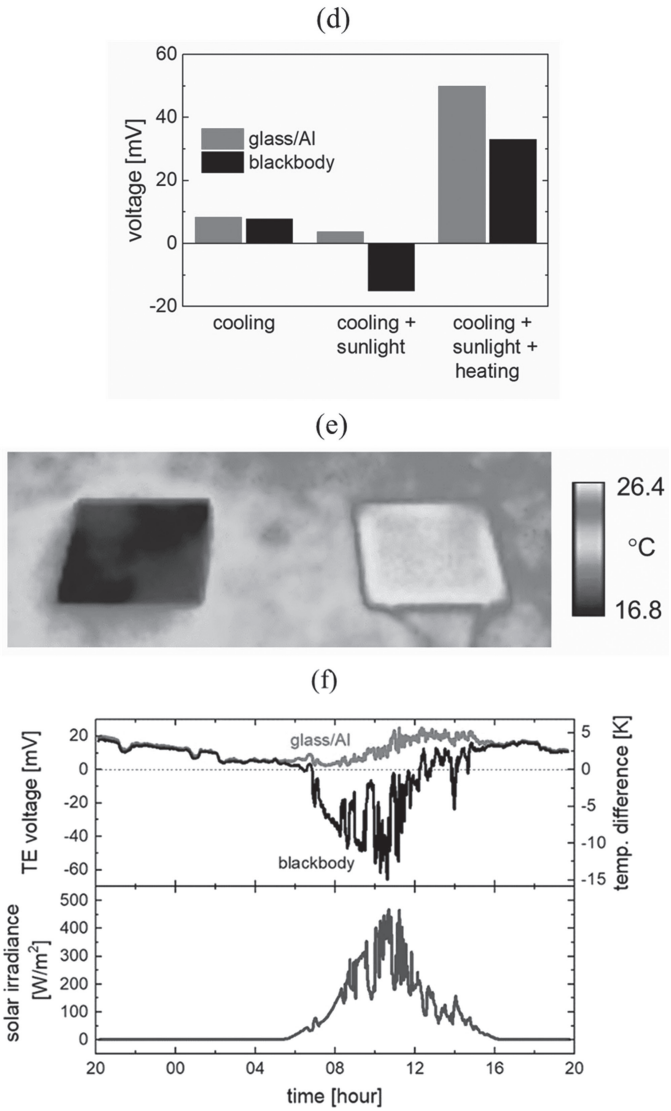

FIGURE 8.2 (*Continued*) (d) A comparison of the thermoelectrical voltage generated under abovementioned three experimental conditions; (e) Thermograph; and (f) measured temperature difference and thermoelectrical voltage of the selective and blackbody thermal emitters under field investigation. Reprinted from *Applied Physics Letters*, **117**, Ishii S, Dao TD, Nagao T, Radiative cooling for continuous thermoelectric power generation in day and night, 013901, with permission from AIP Publishing.

The glass/aluminum emitter has a high reflectivity in the optical range, but a high emissivity in the mid-infrared range.

A blackbody-painted Peltier module and a solar simulator were used to imitate the universe and the sun. As illustrated in Figure 8.2(c), three experimental conditions, simulating a standalone radiative cooling effect, combined radiative cooling and solar heating effect, and combined radiative cooling, solar heating, and conductive heating effect, were trialed. Figure 8.2(d) compares the thermoelectrical voltage generated under abovementioned three experimental conditions. Where there is radiative cooling only, the two samples generated similar voltage. When there are both radiative cooling and solar heating, the one with selective thermal emitter generated positive voltage, whereas the one with the blackbody thermal emitter generated negative voltage with a larger absolute magnitude. Solar heating overwhelmed radiative cooling, resulting in a larger temperature difference and voltage. However, when the samples were heated at the bottom, the former generated a larger voltage than the latter. Top-sided radiative cooling and bottom-sided conductive heating maximized the temperature difference and voltage. When the bottom-sided temperature increased from room temperature to 50 °C, thermoelectrical voltage of the one with a selective thermal emitter increased from 3.8 to 50 mV, whereas the one with the blackbody thermal emitter changed from −15 to 33 mV only. This indicated that a selective thermal emitter could take advantage of bottom-sided heating from waste heat in practice for enhanced radiative-cooling based thermo-electricity generation.

8.3.3 Outdoor Field Investigation of Thermo-Electricity Generation

Then, an outdoor field investigation was conducted to investigate the performance. The selective thermal emitter was radiatively cooled all the time, and the top of the thermoelectricity generator is always cooler than the bottom, thus maintaining continuous thermoelectricity generation. In contrast, the black-paint emitter has a high emissivity across the entire spectrum. The blackbody thermal emitter was radiatively cooled at nighttime but heated by sunlight at daytime. Thus, after sunrise, the top surface temperature increased gradually, and reached the same bottom face temperature gradually. Without vanished voltage, continuous thermoelectricity generation acted as the overwhelming advantage of radiative-cooling based electrical energy harvesting. Figure 8.2(e) shows the thermograph of two devices under field investigation taken in day. As can be seen,

the radiative cooling surface was at a temperature lower than the background, whereas the blackbody was at a higher temperature. Figure 8.2 (f) shows the measured temperature difference and thermoelectrical voltage during field investigation. Note that the temperature difference is positive/negative when the emitter surface is cooler/hotter than the ambient temperature At nighttime, top-to-bottom temperature differences were approximately 2–4 °C for both devices. Consequently, they produced similar thermoelectrical voltage up to 20 mV. At daytime, the temperature difference arrived at 5 °C for the selective thermal emitter, whereas, with a higher top face temperature due to solar heating, it reached a larger value of −15 °C for the blackbody thermal emitter. Hence, the thermoelectricity generator installed by the blackbody thermal emitter generated a larger voltage, up to 60 mV, because solar heating by the blackbody absorber is stronger than radiative cooling by the selective radiative cooler. Moreover, from 1pm to 5pm, the sky was cloudy and inferred from the lower solar irradiance. During this period, the device with a selective thermal emitter recorded a larger thermoelectrical voltage than the one with a blackbody thermal emitter. Furthermore, it generated nearly constant thermoelectrical voltage regardless of weather change.

Later, it was shown that reducing parasitic losses, controlling emitter area and thermal resistance of the thermoelectric generator, and stacking multiple thermoelectric generators are all effective ways to boost the power density. Also, a measured power density exceeding 100 mW/m^2, representing over 2-fold improvement over the previous results, was demonstrated experimentally [50]. Also, a new kind of thermoelectrical energy converter based on the spin Seebeck effect, in which the temperature gradient and the thermoelectrically generated electric field are perpendicular, was suggested for energy harvesting from solar heating and radiative cooling simultaneously [51]. The Spin Seebeck effect induced voltage is proportional to the length of the device, which is perpendicular to the temperature gradient. This means that voltage and power can be increased by simply elongating the device length without forming multitude of serial p-n junctions, as is the case with a conventional thermoelectric device. And, this simplifies the device architecture. A prototype, comprising paramagnetic gadolinium gallium garnet substrate, ferrimagnetic yttrium iron garnet insulator, paramagnetic platinum metal, and blackbody paint light absorber, demonstrated the simultaneous harvesting of radiative cooling and solar heating in the outdoors.

8.4 RESEARCH CHALLENGE IN PASSIVE RADIATIVE COOLING

Geographical variation in the passive radiative cooling performance poses one of the top research challenges in low latitude hot and humid regions. The radiative cooling resource map for the contiguous United Stated showed that the southwestern area had the highest cooling potential of 70 W/m^2, whereas the southeastern had the lowest potential of 30 W/m^2 [52]. Similar maps for China identified that the northwestern area had the highest cooling potential of 70–90 W/m^2, whereas the southeastern had the lowest potential of 10–40 W/m^2 [53, 54]. An investigation of the impact of humidity, cloudiness, and aerosol concentration on radiative cooling performance compared the cooling potential at Stanford and Hong Kong, where the estimated values were 61 W/m^2 and 25 W/m^2 respectively due to climatic difference [55]. Besides, higher solar intensity in Singapore, where the predicted cooling power limit was 30 W/m^2, was identified as the major cause of degraded radiative cooling performance [56]. As such, despite plenty of groundbreaking field investigative reports from North America, some comparative studies conducted elsewhere failed to achieve sub-ambient daytime radiative cooling [57–61]. In Shanghai, where the ambient temperature and relative humidity were above 24 °C and 50 % respectively, nano-particle based solar reflecting thermal radiators were tested, but they remained 3–10 °C above ambient at daytime [57]. In the subtropical city, Hong Kong, Raman's photonic radiative cooler was tested in vacuum and non-vacuum enclosures, but none can replicate sub-ambient daytime radiative cooling [2, 58]. Then a modified titanium oxide photonic radiative cooler and a bio-inspired polymeric radiative cooler were tested with and without shade, and only the shaded ones accomplished sub-ambient daytime radiative cooling [59, 60]. In the tropical country, Singapore, Raman's photonic radiative cooler and an enhanced specular reflective film were assessed. It was concluded that high solar intensity and humidity counteracted the radiative cooling effect [2, 61].

8.4.1 Empirical Sky Temperature Models

Contrary to mainstream deterministic energy balance-based analysis of the variance in radiative cooling performance arising from climatic factors, a new approach by means of probabilistic regression modeling was suggested to establish the correlation between radiative cooling performance and corresponding weather conditions [62]. It is advantageous in tolerancing the uncertainties arising from time varying and uncontrolled

atmospheric uncertainties abundant in field investigation. Meteorological variables like ambient temperature, relative humidity, and cloudiness, quantifying the downwelling atmospheric thermal radiation from the sky, can be lumped into a single parameter of sky temperature. Sky temperature T_{sky} can be viewed as the equivalence of atmospheric thermal intensity I_{sky} in absolute temperature scale, convertible by the Stefan-Boltzmann equation of $I_{sky} = \sigma T_{sky}^4$, where σ = 5.67 × 10^{-8} W/m^2-K^4 is the Stefan-Boltzmann constant. And sky emissivity ε_{sky} is defined by T_{sky} via $\varepsilon_{sky} = (T_{sky}/T_{amb})^4$. As ε_{sky} ranges from 0 to 1, T_{sky} is always lower than T_{amb}. ε_{sky} can be measured by a pyrometer experimentally, simulated by an atmospheric radiative transfer model numerically, and a sky emissivity model empirically. A pyrometer produces an output voltage by scanning in situ infrared radiance within 4.5–100 μm, but it requires careful calibration to eliminate background radiation from buildings and vegetations. An atmospheric radiative transfer model evaluates the atmospheric spectral emissivity within 0.2–100 μm line-by-line upon comprehensive specification of absorbing gases, aerosol, water vapor, cloud characteristics, vertical temperature, and humidity profiles, as well as various secondary atmospheric variables [63, 64]. In contrast, an empirical model is rather simple, correlating ε_{sky} with fundamental meteorological variables measurable by the observatory.

Since the 1910s, plenty of sky temperature models, falling into two categories regarding clear and cloudy skies, have been suggested. Under a clear sky, suspended water vapors act as the primary source of downwelling atmospheric thermal radiation. In 1932, Brunt formulated one of the earliest clear sky temperature models, expressing clear sky emissivity $\varepsilon_{sky,c}$ as

$$\varepsilon_{sky,c} = a_1 + a_2 p_w^{\frac{1}{2}}, \tag{8.16}$$

where a_1 = 0.52 and a_2 = 0.065 are the empirical constants, and p_w is the vapor pressure [65]. Afterwards, various parametric forms were suggested, and published models were also recalibrated. These reports revealed the difficulty in universal sky temperature modeling because the models were established with localized and biased meteorological data drawn from one or several weather stations. A recent revisit on this topic might have analyzed the most comprehensive meteorological and radiation data, collected from seven stations of the Surface Radiation Budget Network in the United

States, located at Goodwin Creek (Mississippi), Bondville (Illinois), Penn State University (Pennsylvania), Fort Peck (Montana), Sioux Falls (South Dakota), Boulder (Colorado), and Desert Rock (Nevada). The meteorological dataset, covering climatic diversity in the northern hemisphere, were used to recalibrate Brunt's model with renewed empirical constants of $a_1 = 0.62$ and $a_2 = 0.056$ [66]. Under a cloudy sky, clusters of liquid phase water and solid phase ices absorb and emit longwave radiation more vigorously than gaseous phase vapors. To cater for additional heat load imposed by clouds, clear sky emissivity ought to be corrected by a factor regarding cloud fraction. A new empirical form of cloudy sky emissivity ε_{sky} was suggested as

$$\varepsilon_{sky} = \varepsilon_{sky,c}\left(1 - b_1 f_c^{b_2}\right) + b_3 f_c^{b_4} \phi^{b_5}, \tag{8.17}$$

where $b_1 = 0.78$, $b_2 = 1$, $b_3 = 0.38$, $b_4 = 0.95$ and $b_5 = 0.17$ are the empirical constants, ϕ is the relative humidity, and f_c is the cloud fraction [66]. In the expression, $\varepsilon_{sky,\,c}$ can be calculated with recalibrated Brunt's clear sky emissivity by Equation (3.1). When $f_c = 0$, it represents the clear sky condition, and ε_{sky}, given by Equation (3.2), is reduced to $\varepsilon_{sky,\,c}$. Hence, cloudy sky temperature model is applicable for all sky conditions.

8.4.2 Correlations Between Sky Temperature Difference and Surface Temperature Reduction

Outdoor field investigations were conducted for photonic radiative and polymeric radiative coolers. For each kind of radiative cooler, one was shadowed by an external shade, and one was exposed to direct sunlight. During the investigations, surface temperatures and site ambient temperature were measured. Meanwhile, ambient temperature, relative humidity, cloud fraction, and solar intensity were collected from neighboring weather stations.

In total, 70 sets of field investigative results were gathered at nighttime, whereas 35 sets were gathered at the peak solar radiance. Then temperature measurements were time averaged. And Figure 8.3(a)–(d) shows the scatterplots of the response variable of surface temperature reduction against predictor variable of sky temperature difference for different materials at nighttime. Surface temperature reduction, as a cardinal indicator of radiative cooling performance, is a reasonable selection for the response variable. Also, sky temperature difference, which is the difference between

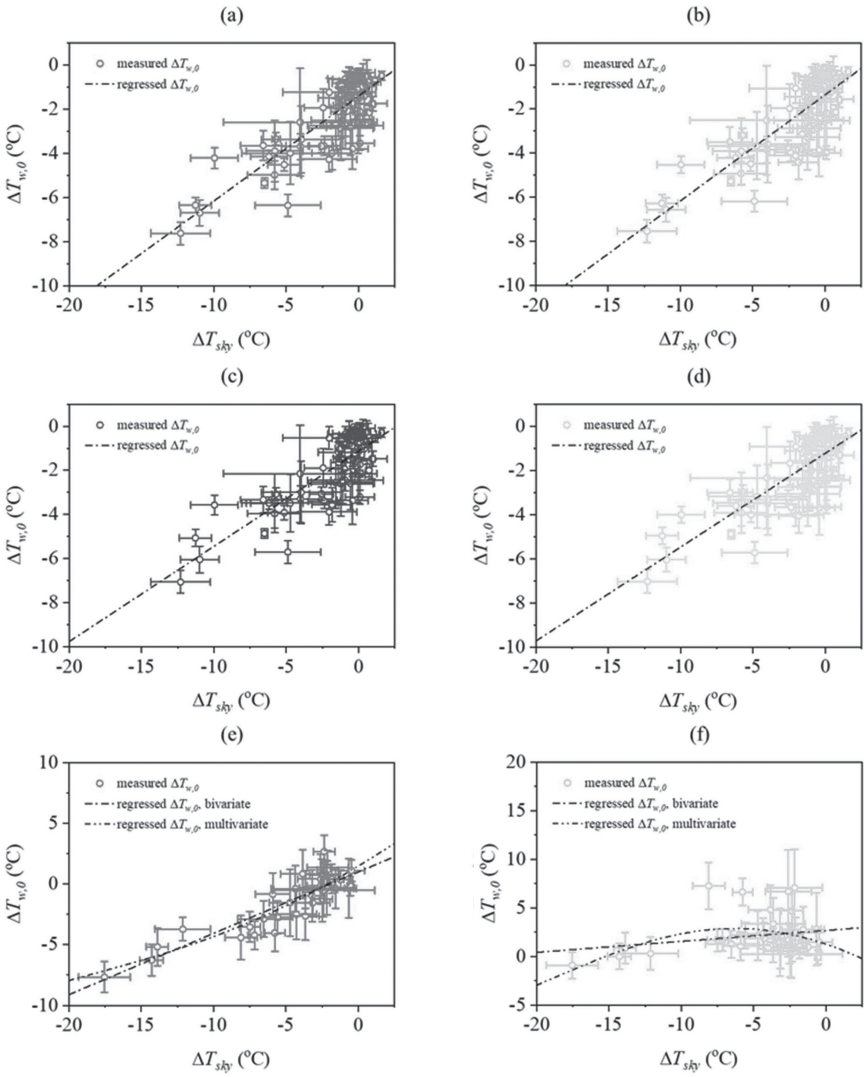

FIGURE 8.3 Scatterplots of surface temperature reduction at nighttime against sky temperature difference and bivariate regression lines for (a) shaded polymeric radiative cooler; (b) unshaded polymeric radiative cooler; (c) shaded photonic radiative cooler; and (d) unshaded photonic radiative cooler. Scatterplots of surface temperature reduction at daytime against sky temperature difference, bivariate and multi-variate regression lines for (e) shaded polymeric radiative cooler; (f) unshaded polymeric radiative cooler.

(*Continued*)

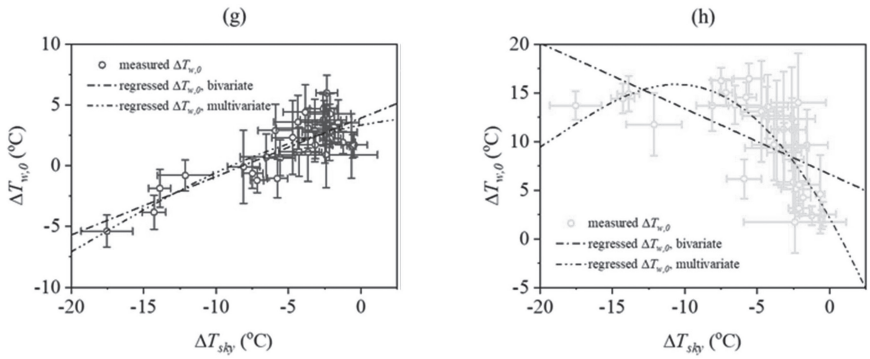

FIGURE 8.3 (*Continued*) (g) shaded photonic radiative cooler; and (h) unshaded photonic radiative cooler. Reprinted from *Renewable Energy*, **211**, Wong RYM, Tso CY, Jeong SY, Fu SC, Chao CYH, Critical sky temperatures for passive radiative cooling, 214–226, Copyright (2023), with permission from Elsevier.

sky temperature and ambient temperature, can be an appropriate choice for the predictor variable. It is because, from an energy balance consideration, net radiative heat exchange by the radiative cooler results from outfluxing emission proportional to the fourth power of surface temperature and inflowing absorption proportional to the fourth power of sky temperature. For small differences among ambient temperature, sky temperature, and surface temperature, they can be expressed as a Taylor expansion about ambient temperature, and thus, net radiative heat exchange can be scaled with a single, lumped meteorological variable of sky temperature difference. From a statistical perspective, each data-pair scatters about the best fitted line. Supposed to be linear, the best fitted lines, based on optimal intercept coefficient and slope coefficient, are plotted in the same figure for reference. Variance of surface temperature reduction and R^2 value estimate the reliability of the regression model, where the former represents the amount of variability inherent in the regression model, and the latter interprets the proportion of variation in surface temperature reduction predictable from the sky temperature difference. The variances after normalization are approximately the same of −0.18 for all specimens, which means climatic factors impact on expected radiative cooling performance, but do not alter the random deviation, and R^2 values lie within 0.63 and 0.7, which denotes a substantial linear correlation between surface temperature reduction and sky temperature difference for nighttime radiative cooling performance.

At daytime, solar absorption imposes an additional heat load on the radiative coolers. Figure 8.3(e)–(h) plots the corresponding scatterplots under the peak solar intensity. Repeating the bivariate linear regression model for data analysis, variances and R^2 values lie within statistically valid ranges for shaded radiative coolers, whereas they appear as tremendous departures between measured datasets and regressed equations, and associated random errors are magnified enormously, but R^2 values are reduced dramatically, questioning the linear coupling between sky temperature difference and surface temperature reduction. Therefore, it is essential to revise the model by introducing an extra predictor variable regarding solar heat load. Obviously, sky temperature difference and solar intensity are not mutually independent variables, but solar intensity should be regarded as a single variable function of sky temperature difference, and its explicit form ought to be pre-determined otherwise. Beer-Lambert law states that [67, 68] spectral radiative extinction traversing a thin layer of medium is proportional to local spectral intensity, number density and extinction cross section of extinctive particles, as well as medium thickness. For the atmosphere composed of multi-component gases and suspended particulates, the contribution of extinction cross section by each species is additive and the integral form of Beer-Lambert law can be written as

$$I(\lambda, s) = I(\lambda, 0) e^{-\int_s \sum_j K_j(\lambda) N_j(s') ds'}. \tag{8.18}$$

Constituent gases, like nitrogen, oxygen, and argon, occupy permanent fractions in the atmosphere, whereas suspended particulates, like aerosols, water vapors, and clouds, are time and space varying in concentration. Complicated extinction mechanism and comprehensive specification of number density and extinction coefficient for each atmospheric constituent throughout the optical path do not facilitate practical implementation of Beer-Lambert law. In many circumstances, it is essential to recognize these changes with respect to climatic parameters like sky temperature rather than their absolute values. Because of a small variation in sky temperature, the term, $\sum_j K_j N_j$, in the Beer-Lambert equation at any sky temperature can be expressed as a Taylor's expansion about a reference sky temperature. And the contributions from water vapors and clouds become the only terms dynamic with sky temperature. Further neglecting spatial variations

in extinction cross-sections of vapors and clouds yields the territorial solar intensity written as $I_{\text{sun}}\left(\Delta T_{\text{sky}}\right) = I_{\text{sun}}^{(0)} e^{-\left(\Delta T_{\text{sky}} - \Delta T_{\text{sky}}^{(0)}\right)\int_S \left(K_{\text{v}}\partial N_{\text{v}}/\partial T_{\text{sky}} + K_{\text{c}}\partial \boldsymbol{N}_{\text{c}}/\partial T_{\text{sky}}\right)ds'}$, where $I_{\text{sun}}^{(0)}$ represents the solar intensity at $T_{\text{sky}}^{(0)}$, which can be as high as 1140 W/m^2 at low-to-mid altitude areas [69]. Admittedly, a constant extinction cross-section assumption may not stand because water vapors are spectrally selective solar absorbers, in which the atomic arrangement of water molecule permits three fundamental vibration modes of symmetry, bending, and anti-symmetry, responsible for multiple solar and near-infrared absorption bands at 940 nm, 1.1 μm, 1.38 μm and 1.87 μm [70]. The integral, $-\int_S (K_{\text{v}}\partial N_{\text{v}}/\partial T_{\text{sky}} + K_{\text{c}}\partial N_{\text{c}}/\partial T_{\text{sky}})ds'$, denotes the exponential declining rate of solar intensity with respect to sky temperature difference. In a semi-empirical treatment, it can be determined by surveying the historical meteorological data pairs of the peak solar intensity against the sky temperature difference, and appraising the slope at any arbitrary sky temperature difference is supposed to be the linear interpolation of two limiting characteristic rates. Hence, the integral can be simplified as $\gamma_1 + 2\gamma_2\Delta T_{\text{sky}}$, where γ_1 and γ_2 are the empirical model constants. They can be determined by minimizing the root-of-squared error between collected dataset and modeling equation. as such, $I_{\text{sun}}\left(\Delta T_{\text{sky}}\right) = I_{\text{sun}}^{(0)} e^{\gamma_0 + \gamma_1\Delta T_{\text{sky}} + \gamma_2\Delta T_{\text{sky}}^2}$ and the multivariate regression equation becomes $\Delta T_{\text{w,0}} = \widehat{\beta}_0 + \widehat{\beta}_1\Delta T_{\text{sky}} + \widehat{\beta}_2 e^{\gamma_0 + \gamma_1\Delta T_{\text{sky}} + \gamma_2\Delta T_{\text{sky}}^2}$. Compared to bivariate regression model, it provides a better fit with scattered data pairs in Figure 8.3(f)–(j), features decreased variances, as well as increased R^2 values, and improves overall interpretability of the statistical model. For shaded radiative coolers, variances range from 1.1 °C to 1.4 °C and R^2 values range from 0.69 to 0.79. The refinement is the least notable because, without the action of direct solar illumination, the bivariate regression model has rationalized radiative cooling performance. For exposed radiative coolers and silicon wafer, the advancement is more significant, revealing the crucial role of solar heat load on cooling performance. Even the polymeric radiative cooler feature reasonably high solar reflectivity variance is reduced to 2.0 °C, and R^2 value is more than doubled, valuing 0.11. The small random uncertainty affirms the reliability of the regression model, whereas the feeble correlation stems from the counter-interaction of radiative cooling and solar heating. For photonic radiative cooler, variance is 3.0 °C and R^2 value is 0.58. The multivariate regression model reduces the random uncertainty but reinforces the correlation between sky temperature difference and surface temperature reduction.

Under a subtropical hot and humid climate, sub-ambient passive radiative cooling is possible providing reconcilable materials with sky window emissivity and solar reflectivity higher than the benchmarked polymeric radiative cooler. A few alternative solution strategies to subtropical and tropical radiative cooling were also proposed. Providing external shading can be the simplest way to block incoming solar radiation and lower surface temperature [59, 60]. In Hong Kong, a radiative cooler with superior spectral selectivity, comprising a solution-derived silicon oxynitride layer sandwiched between a reflective substrate and a self-assembly monolayer of silicon dioxide microspheres narrowband emitter, realized sub-ambient cooling of up to 5 °C in autumn and 2.5 °C in summer [71]. In Singapore, a switchable solar heater radiative cooler with engineered porous structure, enabling the device to serve as an efficient solar reflector and infrared emitter in dry state, as well as an efficient solar heater in wet state, yielded a nighttime cooling power of 61.2 W/m^2 and daytime heating power of 720 W/m^2 [72]. These strategies create a new opportunity for the development of novel and multi-functional radiative cooling materials.

8.5 SUMMARY AND CONCLUSIONS

This chapter reviews passive radiative cooling applications in thermal and electrical energy harvesting. They are important because of plenty of smart and green technological applications toward a carbon neutral built environment. For thermal energy harvesting, chilled water collection by circulating water through a radiative heat exchanger is the simplest form, but it raises critical concerns on thermal and energy conversion performances. A study on a passive radiative fluid cooling system in a controlled environmental facility revealed that water temperature reduction and energy conversion efficiency are always inversely correlated, in which temperature reduction increases with decreasing flow rate but efficiency increases with increasing flow rate. This poses a fundamental difficulty in collecting chilled water in an energy efficient manner. For electrical energy harvesting, thermoelectricity by creating temperature difference through heat dissipation with radiative cooling materials at the cold side can be generated continuously day and night. It demands on the development of high-performance radiative cooling-based thermoelectricity generator delivering power density approaching the theoretical upper limit. However, it must be emphasized that performance of radiative cooling-based devices and systems rely on the weather conditions

heavily. Sky temperature modeling unveils that, the higher the thermal emissivity, the larger is the surface temperature reduction at nighttime, and heavy solar heat load can be absorbed by the radiative coolers at daytime even they feature reasonably high solar reflectivity. Therefore, hot and humid climates are not favorites for passive radiative cooling. This complicates the applications in tropical and subtropical regions, where the cooling demand is the heaviest, though a few overcoming schemes were suggested. Nonetheless, advancement in passive radiative cooling materials and applications will not be stopped and will continuously steer a new shape of our community and society.

REFERENCES

[1] Harrison, A. W., Walton, M. R. (1978). Radiative cooling of TiO_2 white paint. *Solar Energy*, **20**, 185–188.
[2] Raman, A. P., Anoma, M. A., Zhu, L., Rephaeli, E., Fan, S. (2014). Passive radiative cooling below ambient air temperature under direct sunlight. *Nature*, **515**, 540–544.
[3] Chen, Z., Zhu, L., Raman, A., Fan, S. (2016). Radiative cooling to deep subfreezing temperatures through a 24-h day-night cycle. *Nature Communications*, **7**, 13729.
[4] Kou, J., Jurado, Z. Chen, Z., Fan, S., Minnich, A. J. (2017). Daytime radiative cooling using near-black infrared emitters. *ACS Photonics*, **4**, 626–630.
[5] Hossain, M. M., Jia, B., Gu, M. (2015). A metamaterial emitter for highly efficient radiative cooling. *Advanced Optical Materials*, **3**, 1047–1051.
[6] Zou, C., Ren, G., Hossain, M. M., Nirantar, S., Withayachumnankul, W., Ahmed, T., Bhaskaran, M., Sriram, S., Gu, M., Fumeaux, C. (2017). Metal-loaded dielectric resonator metasurfaces for radiative cooling. *Advanced Optical Materials*, **5**, 1700460.
[7] Yu, N., Mandal, J., Overvig, A., Shi, N. N. (2016). Systems and Methods for Radiative Cooling and Heating, US patent: WO2016205717A1.
[8] Zhai, Y., Ma, Y., David, S. N., Zhao, D., Lou, R., Tan, G., Yang, R., Yin, X. (2017). Scalable manufactured randomized glass-polymer hybrid metamaterial for daytime radiative cooling. *Science*, **355**, 1062–1066.
[9] Mandal, J., Fu, Y., Overvig, A. C., Jia, M., Sun, K., Shi, N. N., Zhou, H., Xiao, X., Yu, N., Yang, Y. (2018). Hierarchically porous polymer coatings for highly efficient passive daytime radiative cooling. *Science*, **362**, 315–319.
[10] Peoples, J., Li, X. Y., Lv, Y. B., Qiu, J., Huang, Z. F., Ruan, X. L. (2019). A strategy of hierarchical particle sizes in nanoparticle composite for enhancing solar reflection. *International Journal of Heat Mass Transfer*, **131**, 487–494.
[11] Li, X., Peoples, J., Huang, Z., Zhao, Z., Qiu, J., Ruan, X. (2020). Full daytime sub-ambient radiative cooling in commercial-like paints with high figure of merit. *Cell Reports Physical Science*, **10**, 100221.

[12] Li, X., Peoples, J., Yao, P., Ruan, X. (2021). Ultrawhite $BaSO_4$ paints and films for remarkable daytime subambient radiative cooling, *ACS Applied Mater. Interfaces*, **13**, 21733–21739.
[13] Zhao, B., Hu, M., Ao, X., Chen, N., Pei, G. (2019). Radiative cooling: A review of fundamentals, materials, applications, and prospects. *Applied Energy*, 236, 489–513.
[14] Sun, J., Wang, J., Guo, T., Bao, H., Bai, S. (2022). Daytime passive radiative cooling materials based on disordered media: A review. *Solar Energy Materials and Solar Cells*, **236**, 111492.
[15] Xie, B., Liu, Y., Xi, W., Hu, R. (2023). Colored radiative cooling: Progress and prospects. *Materials Today Energy*, **34**, 101302.
[16] Ali, A. H. A., Taha, I. M. S., Ismail, I. M. (1995). Cooling of water flowing through a night sky radiator. *Solar Energy*, **55**, 235–253.
[17] Erell, E., Etzion, Y. (1999). Analysis and experimental verification of an improved cooling radiator. *Renewable Energy*, **16**, 700–703.
[18] Saitoh, T. S., Fujino, T. (2001). Advanced energy-efficient house (Harbeman house) with solar thermal photovoltaic and sky radiation energies (Experimental results). *Solar Energy*, **70**, 63–77.
[19] Meir, M. G., Rekstad, J. B., Lovvik, O. M. (2002). A study of a polymer-based radiative cooling system. *Solar Energy*, **73**, 403–417.
[20] Dimoudi, A., Androutsopoulos, A. (2006). The cooling performance of a radiator based roof component. *Solar Energy*, **80**, 1039–1047.
[21] Tevar, J. A. F., Castano, S., Marijuan, A. G., Heras, M. R., Pistono, J. (2015). Modelling and experimental analysis of three radioconvective panels for night cooling. *Energy and Buildings*, **107**, 37–48.
[22] Goldstein, E. A., Raman, A. P., Fan, S. (2017). Sub-ambient non-evaporative fluid cooling with the sky. *Nature Energy*, **2**, 17143.
[23] Zhao, D., Aili, A., Zhai, Y., Lu, J., Kidd, D., Tan, G., Yin, X., Yang, R. (2019). Subambient cooling of water: Toward real-world applications of daytime radiative cooling. *Joule*, **3**, 111–123.
[24] Aili, A., Zhao, D., Lu, J., Zhai, Y., Yin, X., Tan, G., Yang, R. (2019). A kw-scale, 24-hour continuously operational, radiative sky cooling system: Experimental demonstration and predictive modelling. *Energy Conversion and Management*, **186**, 586–596.
[25] Zhou, M., Song, H., Xu, X., Shahsafi, A., Qu, Y., Xia, Z., Ma, Z., Kats, M. A., Zhu, J., Ooi, B. S., Gan, Q., Yu, Z. (2021). Vapor condensation with daytime radiative cooling. *Proceedings of National Academy of Science*, **118**, 2019292118.
[26] Haechler, I., Park, H., Schnoering, G., Gulich, T., Rohner, M., Tripathy, A., Milionis, A., Schutzius, T. M., Poulikakos, D. (2021). Exploiting radiative cooling for uninterrupted 24-hour water harvesting from the atmosphere. *Science Advances*, **7**, 3978.
[27] Wang, W., Fernandez, N., Katipamula, S., Alvine, K. (2018). Performance assessment of a photonic radiative cooling system for office buildings. *Renewable Energy*, **118**, 265–277.

[28] Zhang, K., Zhao, D., Yin, X., Yang, R., Tan, G. (2018). Energy saving and economic analysis of a new hybrid radiative cooling system for single-family houses in the USA. *Applied Energy*, **224**, 371–381.
[29] Jeong, S. Y., Tso, C. Y., Zouagui, M., Wong, Y. M., Chao, C. Y. H. (2018). A numerical study of daytime passive radiative coolers for space cooling in buildings. *Building Simulation*, **11**, 1011–1028.
[30] Wong, R. Y. M., Tso, C. Y., Chao, C. Y. H. (2021). Thermo-radiative energy conversion efficiency of a passive radiative fluid cooling system. *Renewable Energy*, **180**, 700–711.
[31] Incropera, F. P., Dewitt, D. P., Bergman, T. L., Lavine, A. S. (2006). *Fundamentals of Heat and Mass Transfer* (6th edition), John Wiley & Sons, United States of America.
[32] Wong, R. Y. M., Tso, C. Y., Chao, C. Y. H. (2021). Corrected radiative cooling power measured by equivalent dissipative thermal reservoir method. *International Journal of Heat and Mass Transfer*, **174**, 121341.
[33] Wong, R. Y. M., Tso, C. Y., Fu, S. C., Chao, C. Y. H. (2023). Field demonstrated extended Graetzian viscous dissipative thermo-photonic energy conversion with a blended MgO/PVDF/PMMA coated glass-PDMS micro-pillar heat exchanger, *International Journal of Heat and Mass Transfer*, **215**, 124520.
[34] Xia, Y., Whitesides, G. M. (1998). Soft lithography. *Annual Review of Materials Science*, **28**, 153–184.
[35] Whitesides, G. M., Ostuni, E., Takayama, D., Jiang, X., Lngber, D. E. (2001). Soft lithography in biology and biochemistry. *Annual Review of Biomedical Engineering*, **3**, 335–373.
[36] Wong, R. Y. M., Tso, C. Y., Fu, S. C., Chao, C. Y. H. (2022). Maxwell-Garnett permittivity optimized micro-porous PVDF/PMMA blend for near unity thermal emission through the atmospheric window. *Solar Energy Materials and Solar Cells*, **248**, 112003.
[37] Grum, F., Luckey, G. W. (1968). Optical sphere paint and a working standard of reflectance. *Applied Optics*, **7**, 2289–2294.
[38] De Sousa Meneses, D., Brun, J., Echegut, P., Simon, P. (2004). Contribution of semi-quantum dielectric function models to the analysis of infrared spectra. *Applied Spectroscopy*, **24**, 100658.
[39] Kelly-Gorham, M. R. K., DeVetter, B. M., Brauer, C. S., Cannon, B. D., Burton, S. D., Bliss, M., Johnson, T. J., Myers, T. L. (2017). Complex refractive index measurement for BaF_2 and CaF_2 via single-angle infrared reflectance spectroscopy. *Optical Materials*, **72**, 743–748.
[40] Palik, E. D. (1991). *Handbook of Optical Constants of Solids (Volume 2)*, Elsevier, United States of America.
[41] Best Research-Cell Efficiencies, https://www.nrel.gov/pv/assets/pdfs/best-research-cell-efficiencies.pdf, accessed in May 2023.
[42] Zhao, D., Yin, X., Xu, J., Tan, G., Yang, R. (2020). Radiative sky cooling-assisted thermoelectric cooling system for building applications. *Energy*, **190**, 116322.
[43] Kwan, T. H., Gao, D., Zhao, B., Ren, X., Hu, T., Dabwan, Y. N. (2021). Integration of radiative sky cooling to the photovoltaic and thermoelectric system for improved space cooling. *Applied Thermal Engineering*, **196**, 117230.

[44] Liu, Y., Hou, S., Wang, X., Yin, L., Wu, Z., Wang, X., Mao, J., Sui, J., Liu, X., Zhang, Q., Liu, Z., Cao, F. (2022). Passive radiative cooling enables improved performance in wearable thermoelectric generators. *Small*, **18**, 2106875.
[45] Khan, S., Kim, J., Roh, K., Park, G., Kim, W. (2021). High power density of radiative-cooled compact thermoelectric generator based on body heat harvesting. *Nano Energy*, **87**, 106180.
[46] Fan, L., Li, W., Jin, W., Orenstein, M., Fan, S. (2020). Maximum nighttime electrical power generation via optimal radiative cooling. *Optics Express*, **28**, 25460.
[47] Zhao, B., Pei, G., Raman, A. P. (2020). Modelling and optimization of radiative cooling based thermoelectric generators. *Applied Physics Letters*, **117**, 163903.
[48] Raman, A. P., Li, W., Fan, S. (2019). Generating light from darkness. *Joule*, **3**, 2679–2686.
[49] Ishii, S., Dao, T. D., Nagao, T. (2020). Radiative cooling for continuous thermoelectric power generation in day and night. *Applied Physics Letters*, **117**, 013901.
[50] Omair, Z., Assawaworrarit, S., Fan, L., Jin, W., Fan, S. (2022). Radiative-cooling based nighttime electricity generation with power density exceeding 100 mW/m^2. *iScience*, **25**, 104858.
[51] Ishii, S., Miura, A., Nagao, T., Uchida, K. (2021). Simultaneous harvesting of radiative cooling and solar heating for transverse thermoelectric generation. *Science and Technology of Advanced Materials*, **22**, 441–448.
[52] Li, M., Peterson, H. B., Coimbra, C. F. M. (2019). Radiative cooling resource maps for the contiguous United States. *Journal of Renewable and Sustainable Energy*, **11**, 036501.
[53] Zhu, Y., Qian, H., Yang, R., Zhao, D. (2021). Radiative sky cooling potential maps of China based on atmospheric spectral emissivity. *Solar Energy*, **218**, 195–210.
[54] Chen, J., Lu, L., Gong, Q. (2021). A new study on passive radiative sky cooling resource maps of China. *Energy Conversion and Management*, **237**, 114132.
[55] Huang, J., Lin, C., Li, Y., Huang, B. (2022). Effect of humidity, aerosol, and cloud on subambient radiative cooling. *International Journal of Heat and Mass Transfer*, **186**, 122438.
[56] Han, D., Fei, J., Li, H., Ng, B. F. (2022). The criteria to achieving sub-ambient radiative cooling and its limits in tropical daytime. *Building and Environment*, **221**, 109281.
[57] Bao, H., Yan, C., Wang, B., Fang, X., Zhao, C. Y., Ruan, X. (2017). Double-layer nanoparticle-based coatings for efficient terrestrial radiative cooling. *Solar Energy Materials and Solar Cells*, **168**, 78–84.
[58] Tso, C. Y., Chan, K. C., Chao, C. Y. H. (2017). A field investigation of passive radiative cooling under Hong Kong's climate. *Renewable Energy*, **106**, 52–61.
[59] Jeong, S. Y., Tso, C. Y., Ha, J. Y., Wong, Y. M., Chao, C. Y. H., Huang, B., Qiu, H. (2019). Field investigation of a photonic multi-layered TiO_2 passive radiative cooler in sub-tropical climate. *Renewable Energy*, **146**, 44–55.
[60] Jeong, S. Y., Tso, C. Y., Wong, Y. M., Chao, C. Y. H., Huang, B. (2019). Daytime passive radiative cooling by ultra emissive bio-inspired polymeric surface. *Solar Energy Materials and Solar Cells*, **206**, 110296.

[61] Han, D., Ng, B. F., Wan, M. P. (2020). Preliminary study of passive radiative cooling under Singapore's tropical climate. *Solar Energy Materials and Solar Cells*, **206**, 110270.
[62] Wong, R. Y. M., Tso, C. Y., Jeong, S. Y., Fu, S. C., Chao, C. Y. H. (2023). Critical sky temperatures for passive radiative cooling. *Renewable Energy*, **211**, 214–226.
[63] Berk, A., Conforti, P., Kennett, R., Perkins, T., Hawes, F., van den Bosch, J. (2014). MODTRAN 6: A major upgrade of the MODTRAN radiative transfer code. *2014 6th Workshop on Hyperspectral Image and Signal Processing: Evolution in Remote Sensing*, 1–4.
[64] Berk, A., Acharya, P. K., Bernstein, L. S., Anderson, G. P., Lewis, P., Chetwynd, J. H., Hoke, M. L. (2008). Band model method for modeling atmospheric propagation at arbitrarily fine spectral resolution. US patent no: 7433806.
[65] Brunt, D. (1932). Notes on radiation in the atmosphere I. *Quarterly Journal of the Royal Meteorological Society*, **58**, 389–420.
[66] Li, M., Jiang, Y., Coimbra, C. F. M. (2017). On the determination of atmospheric longwave irradiance under all-sky conditions. *Solar Energy*, **144**, 40–48.
[67] Liou, K. N. (2002). *An Introduction to Atmospheric Radiation*, 2nd edition. Elsevier, United States of America.
[68] Wallace, J. M., Hobb, P. V. (2006). *Atmospheric Science. An Introductory Survey*, 2nd edition. Elsevier, Canada.
[69] Meinel, A. B., Meinel, M. P. (1976). *Applied Solar Energy. An Introduction*. Addison-Wesley, United States of America.
[70] Liou, K. N., Yang, P. (2016). *Light Scattering by Ice Crystals, Fundamental and Applications*, Cambridge University Press, United Kingdom.
[71] Lin, C., Li, Y., Chi, C., Kwon, Y. S., Huang, J., Wu, Z., Zheng, J., Liu, G., Tso, C. Y., Chao, C. Y. H., Huang, B. (2022). A solution-processed inorganic emitter with high spectral selectivity for efficient subambient radiative cooling in hot humid climates. *Advanced Materials*, **34**, 2109350.
[72] Fei, J., Han, D., Ge, J., Wang, X., Koh, S. W., Gao, S., Sun, Z., Wan, M. P., Ng, B. D., Cai, L., Li, H. (2022). Switchable surface coating for bifunctional passive radiative cooling and solar heating. *Advanced Functional Materials*, **32**, 2203582.